Journal Pre-proof

Evanescent Lamb waves in viscoelastic phononic metastrip

Wei Guo, Shu-Yan Zhang, Yan-Feng Wang, Vincent Laude, Yue-Sheng Wang

PII: S0020-7403(22)00628-2
DOI: https://doi.org/10.1016/j.ijmecsci.2022.107748
Reference: MS 107748

To appear in: *International Journal of Mechanical Sciences*

Received date : 11 June 2022
Revised date : 27 August 2022
Accepted date : 12 September 2022

Please cite this article as: W. Guo, S.-Y. Zhang, Y.-F. Wang et al., Evanescent Lamb waves in viscoelastic phononic metastrip. *International Journal of Mechanical Sciences* (2022), doi: https://doi.org/10.1016/j.ijmecsci.2022.107748.

Evanescent Lamb waves in viscoelastic phononic metastrip

Wei Guo,[1] Shu-Yan Zhang,[2] Yan-Feng Wang,[1,*] Vincent Laude,[3] and Yue-Sheng Wang[1,2]

[1]*School of Mechanical Engineering, Tianjin University, 300350 Tianjin, China*

[2]*Institute of Engineering Mechanics, Beijing Jiaotong University, Beijing 100044, China*

[3]*Institut FEMTO-ST, CNRS, Université Bourgogne Franche-Comté, Besançon 25030, France*

In this paper, the propagation of evanescent Lamb waves in the one-dimensional viscoelastic phononic metastrip is studied. Complex band structures and transmission spectra are calculated by using the finite element method. The effect of viscosity is included according to the Kelvin-Voigt model. Two types (namely H-type and I-type) of metastrips are fabricated in either steel or epoxy. A theoretical model is developed to predict the distribution of the displacements of evanescent waves in the finite metastrip. The effect of different cutting forms on the complex band structure is also investigated. It is found that the spatial attenuation of evanescent waves is clearly observed in both simulation and measurement. Numerical and experimental results agree well for steel metastrips when only the elastic stiffness matrix is considered, whereas good agreement for epoxy metastrips is achieved when viscoelasticity is taken into account. The displacement distribution of evanescent waves can be accurately predicted from the two least evanescent waves identified in the complex band structure. Different slicing forms for the metastrip result in the reconstruction of evanescent waves, leading to the opening or closing of bandgaps. The present work lays the numerical and experimental foundation for practical application of phononic metastrips.

I. INTRODUCTION

Phononic crystals (PCs) are composed of materials with different properties arranged periodically in space[1–5]. The most striking feature of PCs is the band gap, inside which wave propagation is prohibited[6–9]. This feature has led to various applications, such as acoustic insulation[10–12], sound isolation[13–15] and filtering[16,17]. Defect PCs can also be used to design waveguides[18–21] or energy harvesting devices[22–24]. According to the real band structure, bandgaps appear when there are no dispersion curves for a particular frequency range[25]. However, according to energy conservation, waves cannot disappear inside a bandgap. Then, then how do waves transform? Actually, evanescent waves exist in the bandgap and are characterized by the complex band structure[26,27]. The relationship between the real part of the wave number and the frequency in the complex band structure is the dispersion, whereas the relationship between the imaginary part of the wave number and the frequency characterizes attenuation on propagation[28].

In addition to evanescent bulk waves[29–32], complex band structures are also widely used for studying evanescent Lamb waves. Some investigations only focus on flexural waves[33,34]. Han et al calculated the complex band structure of the phononic Euler beam by modifying the transfer matrix method[35], where the state parameters in the transfer matrix method are replaced by initial parameters. Liu and Hussein investigated flexural wave propagation in periodic Timoshenko beams[36]. Effects of various types and consequences of periodicity on the complex band structure have been discussed. Airoldi and Ruzzene designed a tunable one-dimensional metamaterial beam using periodic shunted piezoelectric patches[37]. They showed that a compromise in the resistance should be struck between bandwidth and attenuation, determined by the minimum imaginary part of the wave number. Furthermore, there are also studies focusing on the general Lamb waves. Oudich and Assouar calculated the complex band structure of two-dimensional phononic plates by using the extended plane wave expansion method[38]. The influence of the plate thickness on evanescent waves, including their polarization, was discussed. Gao et al investigated evanescent waves propagation in periodic nested acoustic black hole structures. Different attenuations of flexural and longitudinal waves were characterized by complex band structures and verified experimentally[39].

In practice, solid components are not ideally elastic. Viscosity might exist to some extent, especially for polymers[40–46]. According to the viscoelastic model, the existing studies can be classified into two types. The first type is the generalized Maxwell model. The generalized Maxwell model consists of several spring-dampers connected in parallel; it takes into account the relaxation time of viscoelastic materials. Li et al discussed the complex viscoelastic properties of three-dimensional metamaterials and the effect of thickness and shape of the hole on the attenuation of Bloch waves[47]. Yi et al described the mechanical response of a viscoelastic metamaterial composed of epoxy resin and rubber. They found that by adjusting the mass of the two oscillators in the cell, a quasi-bandgap is created, which results in a wider isolation bandwidth[48]. Lewińska et al studied a locally resonant acoustic metamaterial consisting of tungsten, epoxy and rubber and found that the viscoelastic material affects both the band gap location but also the attenuation of waves at frequencies around the band gap[49]. We then focus on the Kelvin-Voigt (K-V) viscoelastic models, where a frequency-dependent loss is equivalently added to the imaginary part of the modulus. Collet et al calculated the two-dimensional complex band structure of a plate and used the minimum value of the ratio of the imaginary part of the wave number to the amplitude of the wave number at the same frequency to estimate the attenuation of evanescent waves in the band gap[50]. Krushynska et al used the K-V model and the generalized Maxwell model to calculate dissipative solid acoustic metamaterials consisting of rubber. By comparing these two viscoelastic models it is found that the Kelvin-Voigt model provides reliable results from medium to high frequencies[51]. Lou et al investigated longitudinal wave propagation in viscoelastic composite rods. Coupling of the viscosity of the host material and of the damping of the resonator is helpful to widen the band gap and enhance wave attenuation[52]. Krushynska et al compared the elastic model, the K-V model and the generalized Maxwell model to predict experimentally measured viscoelastic curves, revealing the correlation between viscosity of the plate and the transmission spectrum measured experimentally[53]. The above references further investigated the application of viscoelastic models to viscoelastic materials. However, these articles rarely combine the complex band structure and the transmission spectrum of viscoelastic materials to analyze the propagation of evanescent waves in the plate. Furthermore, few experiments have been conducted to compare with the numerical transmission modes.

Recently, increasing attention has been paid to one-dimensional phononic metastrips cut from a slab[54–56]. This setup implies two more free boundaries compared to the usual slab[57]. Efforts have been made to enlarge bandgaps for Lamb waves by strengthening Bragg scattering[58], or coupling Bragg scattering and local resonance[59]. Tunable manipulation of elastic waves was also realized by fluid fillings through fluid-solid interaction[60].

In this paper, we focus on the propagation of evanescent waves in viscoelastic metastrips cut from an epoxy perforated with periodic rectangular holes. Complex band structures and transmission spectra of the metastrips are calculated using the finite element method. Viscoelasticity is introduced by considering the Kelvin-Voigt model. The distribution of displacements of evanescent waves are imaged by using a vibrometer. A theoretical model is developed that predicts accurately the displacement distribution in transmission mode. The effects of the slicing form on the complex band structure are discussed. For comparison, metastrips cut from a lossless steel slab are also investigated.

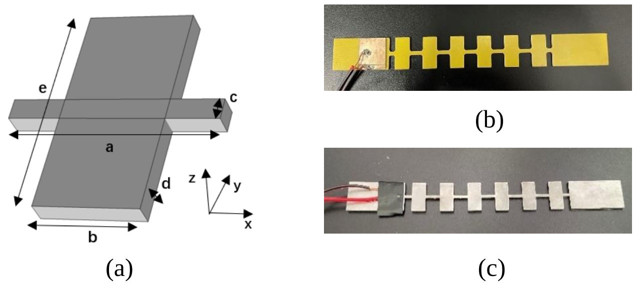

Figure 1: Unit cell (a) and photographs of the H-type epoxy metastrip (b) and steel metastrip (c). Geometric parameters of the unit cell are $a = 20$ mm, $b/a = 0.5$, $c/a = 0.1$, $d/a = 0.1$, and $e/a = 1$.

II. NUMERICAL AND EXPERIMENTAL METHODS

In this section, the numerical method used for the computation of complex band structure is given along with the K-V model. Numerical and experimental evaluation of the distribution of displacements in metastrips is also presented.

First, we introduce the K-V model to characterize the viscoelastic behavior of materials. The stiffness tensor $\widetilde{\mathbf{C}}$ can be expressed as[61]

$$\widetilde{\mathbf{C}} = \mathbf{C} + \imath\omega\boldsymbol{\eta}, \tag{1}$$

with $\mathbf{C}$ and $\boldsymbol{\eta}$ the elastic tensor and the viscoelastic tensor, respectively. For harmonic wave propagation in the viscoelastic solid, the dynamic equilibrium equation is[62]:

$$\rho\omega^2\mathbf{u}(\mathbf{r},\mathbf{k}) + \nabla\cdot[\widetilde{\mathbf{C}} : \nabla^s\mathbf{u}(\mathbf{r},\mathbf{k})] = \mathbf{0}, \tag{2}$$

where ρ is the mass density, ω is the angular frequency, $\mathbf{u} = (u, v, w)^T$ is the displacement vector , $\mathbf{r} = (x, y, z)$ is the coordinate vector, $\mathbf{k} = (k_x, k_y, k_z)$ is the wave vector, and $\nabla^s\mathbf{u}(\mathbf{r}) = 1/2(\nabla\mathbf{u}(\mathbf{r}) + (\nabla\mathbf{u}(\mathbf{r}))^T)$. According to the Bloch theorem, the displacement has the following form:

$$\mathbf{u}(\mathbf{r},\mathbf{k}) = \mathbf{u}_{\mathbf{k}}(\mathbf{r})e^{-\imath\mathbf{k}\mathbf{r}}, \tag{3}$$

where $\mathbf{u}_{\mathbf{k}}(\mathbf{r})$ is a periodic function of coordinate. When viscosity is introduced, all propagating waves become evanescent and should be characterized using complex band structures. For this purpose, the wavenumber can be isolated in the governing equation by substituting Eq. (3) into Eq. (2). We obtain the generalized wave equation:

$$\rho\omega^2\mathbf{u}_n(\mathbf{r}) + \nabla\cdot[\widetilde{\mathbf{C}}:\nabla^s\mathbf{u}_\mathbf{k}(\mathbf{r})] - \imath\mathbf{k}\cdot[\widetilde{\mathbf{C}}:\nabla^s\mathbf{u}_\mathbf{k}(\mathbf{r})] - \imath(\nabla\cdot\widetilde{\mathbf{C}})\cdot[\mathbf{u}_\mathbf{k}(\mathbf{r})\otimes\mathbf{k}] \\ +\mathbf{k}\cdot\widetilde{\mathbf{C}}\cdot[\mathbf{u}_\mathbf{k}(\mathbf{r})\otimes\mathbf{k}] = \mathbf{0}. \tag{4}$$

Since both k and ω are involved in the governing equation, we can solve for the real band structure by choosing ω as the eigenvalue and sweeping k along the boundary of irreducible Brillouin zone.

Alternatively, we can also calculate the complex band structure by choosing k as the eigenvalue and by sweeping ω in the frequency range of interest. Commonly used methods for calculating the complex band structure include for instance the transfer matrix method[63], the extended plane wave expansion method[64], and the finite element method[61]. In this paper, we use the partial differential equation (PDE) module of the finite element software COMSOL to calculate the complex band structure. We set $\mathbf{k} = k\boldsymbol{\theta}$, with $\boldsymbol{\theta} = (\cos\phi, \sin\phi\cos\theta, \sin\phi\sin\theta)$, where $k = |\mathbf{k}|$ and $\boldsymbol{\theta}$ denotes the unit vector parallel to the propagation direction of the elastic wave. ϕ is the angle of the unit vector with the x-axis and θ is the angle of projection of the unit vector in the yz-plane with the y-axis. First we focus on the one-dimensional periodic (H-type) metastrip with unit cell shown in Fig. 1. The unit cell has a relatively large mass block and narrow connectors. Therefore it is adapted to the generation of resonant band gaps[65]. Considering wave propagation along the direction of periodicity, we have $\phi = \theta = 0$ and thus $\mathbf{k} = (k_x, 0, 0)$. The governing equation for the PDE module has the following form:

$$-\rho\omega^2\mathbf{u} + \nabla\cdot(-\widetilde{\mathbf{C}}\nabla\mathbf{u} - \boldsymbol{\alpha}\mathbf{u}) + \boldsymbol{\beta}\cdot\nabla\mathbf{u} + \boldsymbol{\gamma}\mathbf{u} = \mathbf{0}, \tag{5}$$

with $\boldsymbol{\alpha}$, $\boldsymbol{\beta}$, $\boldsymbol{\gamma}$ coefficient matrices to be determined. Comparing Eq. (4) and Eq. (5) we obtain $\boldsymbol{\alpha} = -\imath\widetilde{\mathbf{C}}\cdot\mathbf{k}$, $\boldsymbol{\beta} = \imath\mathbf{k}\cdot\widetilde{\mathbf{C}}$ and $\boldsymbol{\gamma} = -\mathbf{k}\cdot\widetilde{\mathbf{C}}\cdot\mathbf{k}$. Periodic boundary conditions are applied on the surfaces perpendicular to the x-axis direction

$$\mathbf{u}_\mathbf{k}(\mathbf{r}) = \mathbf{u}_\mathbf{k}(\mathbf{r}+\mathbf{a}), \tag{6}$$

and the remaining surfaces are left free. A triangular mesh is first used for the top surface with element size in the range $a/100 - a/10$. Then a swept mesh is generated to divide the geometric model into 4 layers in the thickness direction. A similar process for the use of the PDE module can be found in Ref.[61] for bulk waves.

Furthermore, experimental measurements are carried out to investigate the propagation of evanescent waves. An asymmetric wave source is applied to the left of the metastrip by attaching a piezoelectric patch on the strip in Fig. 1(b) and (c). The response is collected on the right part of the metastrip by using a Polytec scanning vibrometer. The detailed experimental process can be found in Ref.[60]. For comparison, we also calculate the transmission spectrum of a three-dimensional finite metastrip by applying an out-of-plane excitation. We define the transmission in decibel units by

$$F = 20\log_{10}\left(\frac{\int_{S_1}|U_1|dS}{\int_{S_2}|U_0|dS}\right), \tag{7}$$

where U_1 is the total displacement received on the right side of the metastrip (S_1) and $U_0 = 1$ is the z-polarized wave source at the left side (S_2). The length of the numerical model is slightly smaller than that for experiment to reduce the calculation cost, but accuracy is not affected.

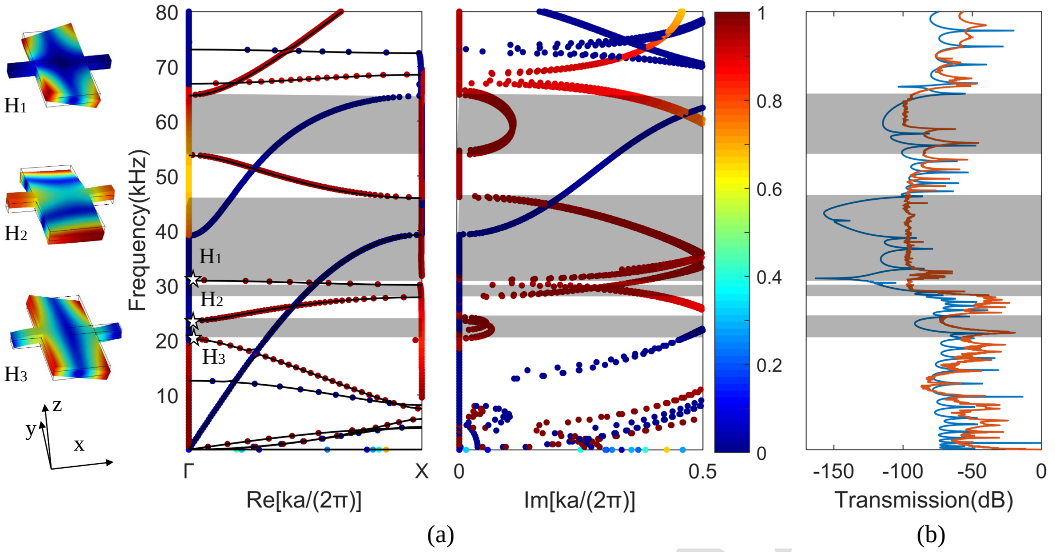

Figure 2: Complex band structure (a) and transmission spectrum (b) of the H-type steel metastrip. The left and right parts in panel (a) show the variation of frequency with the real and imaginary wave number, respectively. Only the elastic model is considered. The color scale indicates the polarization of waves from in-plane modes (blue) to out-of-plane modes (red). The black solid line is the real band structure of the elastic model. The gray area represents the band gap for out-of-plane waves. The distributions of the z-polarized displacement at the marked points H_1, H_2 and H_3 in panel (a) are also presented. Numerical and experimental transmissions are presented in panel (b) using blue and red lines, respectively.

III. EVANESCENT WAVE IN ELASTIC METASTRIP

Before introducing viscoelasticity, we first investigate evanescent wave propagation in the bandgap of the elastic steel metastrip. The material parameters of the elastic steel are $C_{44} = 80.769$ Gpa, Poisson's ratio $\nu = 0.3$ and mass density $\rho = 7850$ kg/m^3. The complex band structure of the H-type steel metastrip can be obtained by following the process in section II with viscosity neglected. The results are shown in Fig. 2. In order to distinguish between different polarized modes, we further calculate the polarization amount p_w for out-of-plane waves:

$$p_w = \frac{\int_V |w|^2 dV}{\int_V (|u|^2 + |v|^2 + |w|^2) dV}. \tag{8}$$

For comparison, the real band structure of the elastic metastrip is also presented with the black solid line in Fig. 2. It is obviously found that the real part of the complex band structure is exactly the same as the real band structure with the imaginary part being uniformly zero. Hence this study also serves to verify the calculation of complex band structures. In addition to those waves that are propagating with no attenuation in the structure, the imaginary part

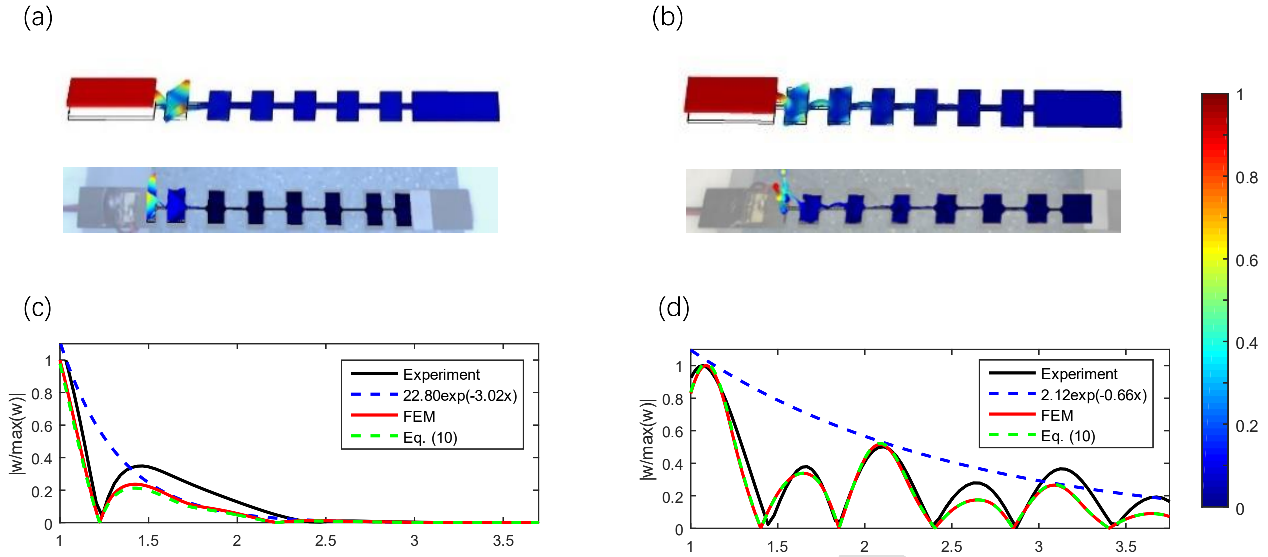

Figure 3: Attenuation of evanescent waves in H-type steel metastrip. Panels (a) and (b) show the numerical and experimental transmission modes of finite steel metastrips at 35 kHz and 60 kHz, respectively. The color scale represents the amplitude of normalized displacement. Panels (c) and (d) show the displacement distribution along the central line on the top surface of the metastrip at 35 kHz and 60 kHz respectively. The numerical and experimental displacement distribution along the central line of the top surface is shown in solid line in the top part of panel. The black and red lines indicate the displacement distribution obtained from experimental and simulations, respectively. The green dashed lines represent the displacement distributions predicted from Eq. (10) with $\phi_1 = 0.5$, $k_1 = -9.42 - 3.02i$, $\phi_2 = 0.5$, $k_2 = -3.14 - 3.01i$ in (a) and $\phi_1 = 0.5$, $k_1 = -0.66i$, $\phi_2 = 0.5$, $k_2 = -6.28 - 0.66i$ in (b). The blue dashed line represents the exponential-like decay of the measured displacement fitted by the minimum imaginary wavenumber in the complex band structure.

also presents 4 frequency ranges where non-zero values exist and are marked by red dots: $20.2 - 23.5$ kHz, $27.8 - 30.1$ kHz, $30.8 - 45.9$ kHz and $53.7 - 64.6$ kHz. They are band gaps for out-of-plane waves, where only evanescent waves exist. Fig. 2(b) presents numerical and experimental transmission spectra of the finite metastrip. It is observed that numerical and experimental results agree very well. The transmission becomes small in the 4 ranges characterized by the complex band structure. This result indicates that it is reasonable to use the elastic model to predict accurately the transmission properties of the steel metastrip. It is also noted that there are many transmission peaks in the transmission spectrum. They correspond to the resonance of the finite elastic metastrip.

A relatively flat band around 30 kHz is observed in the real part of the complex band structure. The z-polarized displacement distribution at point H_1 is given in Fig. 2. Vibrations on the two sides of the central beam are in phase opposition, so mode H_1 can not be excited by applying a symmetric harmonic plane wave source. This band is thus identified as a deaf band[66,67]. The deafness of this band is also verified by the numerical transmission spectra in Fig. 2(b) where only very small transmission is observed around 30 kHz. A small transmission peak is found in the experimental transmission around that frequency, however. This might be owing to the fact that the piezoelectric patch is not completely parallel to the metastrip, so that spurious in-plane waves are excited and collected by the

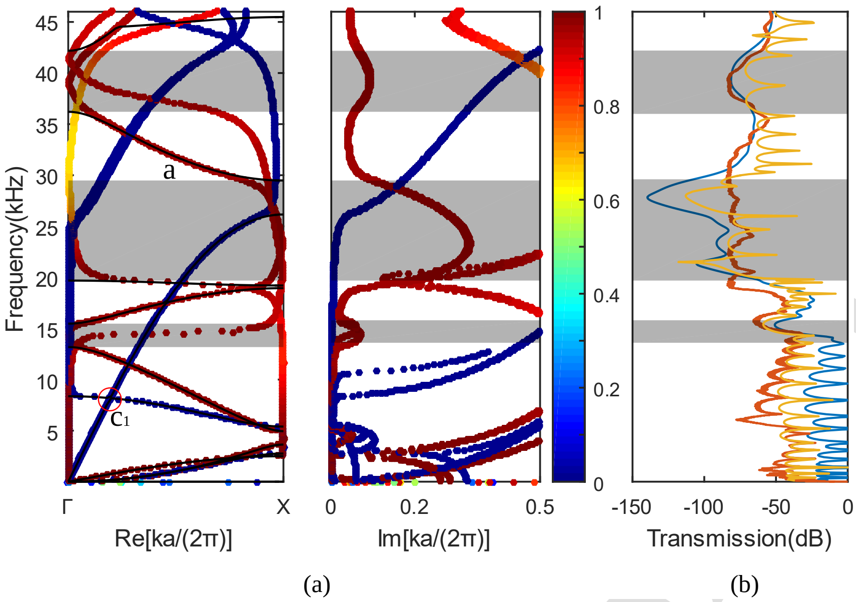

Figure 4: Complex band structure (a) and transmission spectrum (b) of the H-type epoxy metastrip. The left and right parts in panel (a) show the variation of frequency with the real and the imaginary wave number, respectively. Viscosity is introduced according to the K-V model. The color scale indicates the polarization of waves from in-plane modes (blue) to out-of-plane modes (red). The black solid line is the real band structure of the corresponding elastic model. The gray area represents the band gap for out-of-plane waves in the real band structure. The experimental transmission is presented in panel (b) with the red line. For comparison, numerical transmissions obtained by using the K-V model and the corresponding elastic model are presented with the blue and the yellow lines, respectively.

vibrometer.

To further investigate evanescent waves, we select two frequency points (35 kHz and 60 kHz) inside the bandgap and illustrate in Fig. 3 the displacement distribution at the top surface of the structure. It is observed that vibrations mainly concentrate on the unit cells close to the wave source, and the other unit cells show almost no vibrations. This spatial decay, observed in both simulation and experiment, is the typical behavior of evanescent waves. Meanwhile, vibrations are found to propagate further in Fig. 3(b) compared to Fig. 3(a). To quantitatively evaluate the decay, we plot the displacement distribution along the central line of the top surface in Figs. 3(c) and (d), respectively. Numerical and experimental results are shown using black and red lines, respectively. Both results are found to decay in an exponential way. The decay is related to the minimum imaginary wavenumber in the complex band structure[68], as indicated by the dashed lines. The minimum imaginary wavenumber at 35 kHz is 3.02, larger than that at 60 kHz (0.66). So the vibration decays faster at 35 kHz.

IV. EVANESCENT WAVE IN VISCOELASTIC METASTRIP

In this section, we turn our attention to the epoxy metastrip. As epoxy is a kind of polymer, its viscosity is generally more pronounced than that of common solids (e.g. steel), making it more difficult to predict the wave response with

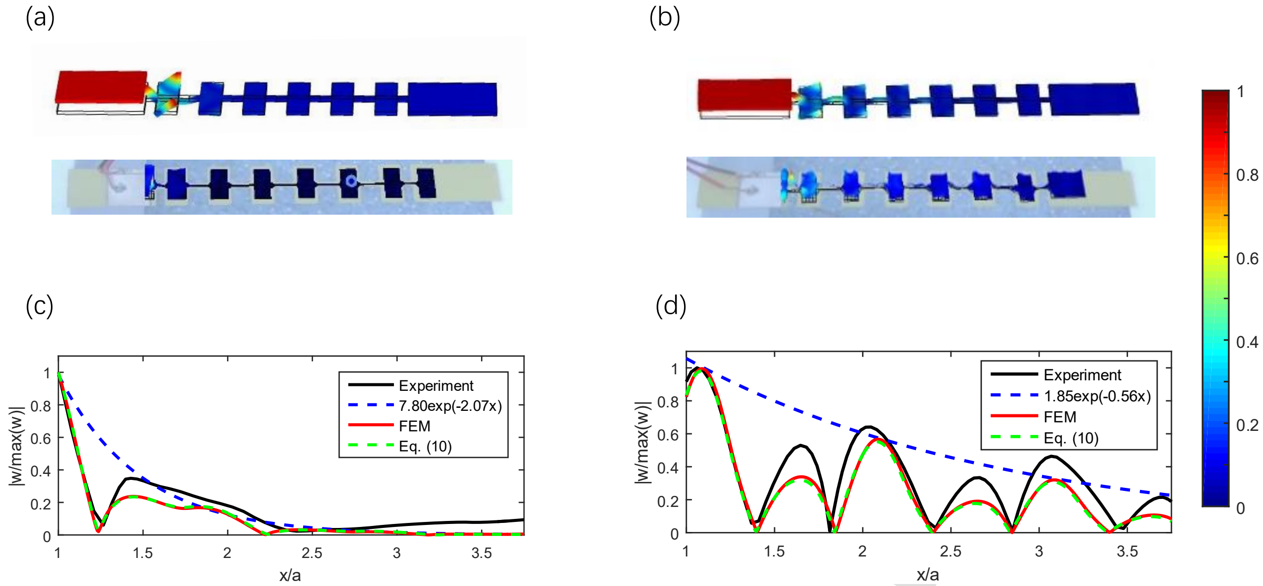

Figure 5: Attenuation of evanescent waves in the H-type epoxy metastrip. Panels (a) and (b) show the numerical and experimental transmission modes of finite steel metastrips at 24 kHz and 40 kHz, respectively. The color scale represents the amplitude of the normalized displacement. Panels (c) and (d) show the displacement distribution along the central line on the top surface of the metastrip at 24 kHz and 40 kHz. The numerical and experimental displacement distributions along the central line of the top surface are shown with a solid line in the top part of panel. The black and the red lines indicate the displacement distribution obtained from experimental and simulations, respectively. The green dashed lines represent the displacement distributions predicted from Eq. (10) with $\phi_1 = 0.66$, $k_1 = -3.11 - 2.03i$, $\phi_2 = 0.33$, $k_2 = 9.46 - 2.06i$ in (a) and $\phi_1 = 0.5$, $k_1 = 0.07 - 0.55i$, $\phi_2 = 0.5$, $k_2 = 6.35 - 0.56i$ in (b). The blue dashed line represents the exponential-like decay of the measured displacement fitted by the minimum imaginary part of the wave number in the complex band structure.

an elastic model. The K-V model is thus used in the numerical simulation and for comparison with experiment. The material parameters used for epoxy are $C_{44} = 8.51$ GPa, $\eta_{44} = 2.128 \times 10^3$ Pa$\cdot$s, Poisson's ratio $\nu = 0.41$ and mass density $\rho = 2038$ kg/m^3. We plan to measure material parameters for instance using a dynamic mechanical analyzer (DMA) in the future.

The complex band structure and the transmission spectrum of the epoxy metastrip computed including the K-V model are shown in Fig. 4(a). The real band structure calculated by using the elastic model is additionally presented for comparison. Since we consider the same unit cell, the real band structure for elastic epoxy is apparently the same with that for steel, but compressed to lower frequencies. Three bandgaps for out-of-plane waves are observed and marked in gray in the elastic case. The sharp corners at the bandgap edge of the real band structure becomes rounded in the complex band structure when viscoelasticity is considered. As frequency increases, the effect becomes more obvious. The minimum imaginary part gets larger compared to the results for steel in Fig. 2(a), suggesting a larger attenuation even in the passing bands. Fig. 4(b) shows the numerical and experimental transmission for a finite epoxy metastrip. The blue and yellow lines present the numerical results of the K-V model and the elastic model, respectively, whereas the red line presents the experimental result. It is found that the transmission obtained by using the K-V model and experiment agree very well. We have further considered the generalized Maxwell model in the computation of the transmission[51], but comparison with experiment was not found to be improved. Details can be found in Appendix A. Transmission peaks appearing in the elastic spectrum are washed out in the relative high frequency range of the viscoelastic spectrum in both simulation and measurement. This is attributed to the increasing effect of viscosity[69], which is not observed in the transmission of Fig. 2(b). Bandgap edges become blurry in the transmission spectrum as compared to steel.

Figs. 5(a) and (b) illustrate the displacement distribution for epoxy at 24 kHz and 40 kHz. The variations of displacement along the central line are shown in Figs. 5(c) and (d). Vibrations are found to decay in an exponential way in both cases. Experimental results agree well with numerical simulation when the K-V model is selected. The amplitude attenuation can be well fitted by using the minimum imaginary wavenumber determined from the complex band structure. Hence, the evanescent behavior is correctly characterized using the K-V model.

V. THEORETICAL MODEL TO PREDICT DISPLACEMENT DISTRIBUTION OF EVANESCENT WAVE

In this section, a theoretical model is proposed to predict the modal distribution of evanescent wave in the metastrip. According to the theory of diffraction gratings[30], the diffracted field is a superposition of harmonic waves with different diffraction orders, some of them evanescent. The appearance of evanescent waves in the periodic metastrip can be understood in a similar way. Since there exists many evanescent modes at any frequency, the evanescent field can be described as:

$$w(x, y) = \sum_{n=1}^{m} \phi_n w_n(x, y) e^{-ik_n x}, \tag{9}$$

where w_n represent the displacement fields extracted from the n_{th} order eigenmodes in the complex band structure with wavenumber k_n. ϕ_n is a weighting coefficient for each evanescent wave. Since evanescent waves decay very fast, we consider only the lowest two orders to approximate the transmission mode. Eq. (9) is then rewritten

$$w(x, y) = \phi_1 w_1(x, y) e^{-ik_1 x} + \phi_2 w_2(x, y) e^{-ik_2 x}. \tag{10}$$

Figs. 3 and Figs. 5 show the predicted displacement distribution from Eq. (10) with the green line. The numerical and predicted results match perfectly with the lowest two orders of evanescence. They agree convincingly with the experimental distributions. The remaining small discrepancies might be owing to slightly different settings in the experiment and simulation. This indicates that the oscillations of the displacement distributions, rather than the decaying trend, are accurately predicted by Eq. (10). This prediction is very helpful for the practical design of phononic metastrips. Furthermore, it is also noted that accurate material properties should be considered in the calculation of complex band structures, especially for polymer with large viscosity.

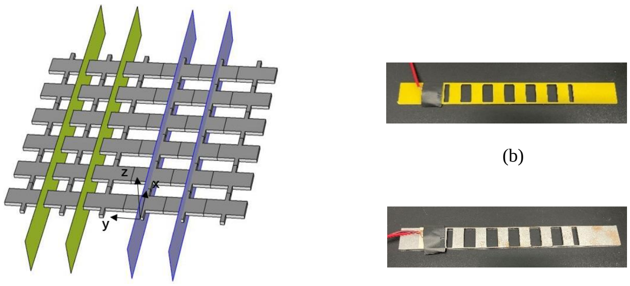

(a) (b) (c)

Figure 6: Schematic diagram of different metastrips cut from a slab and the I-type metastrips fabricated for experiments. (a) The yellow and blue cut areas indicate the H-type and I-type metastrips, respectively. (b) The metastrip made of epoxy. (c) The metastrip made of steel.

VI. I-TYPE METASTRIPS

In this section we study the effect of different cutting forms on the behavior of evanescent waves, with impact on the complex band structure and the transmission spectrum[58,70]. Two different forms, as shown in Fig. 6, are considered. The yellow areas in Fig. 6(a) show the cut form of the H-type sample in Fig. 1, while the blue areas show the same for the I-type sample. The I-type metastrips fabricated in epoxy and steel are shown in Figs. 6(b) and (c).

Complex band structures and transmission spectra of the I-type metastrips are shown in Fig. 7 for epoxy and Fig. 8 for steel, respectively. It is found that evanescent waves are reconstructed for different cutting forms, leading to the generation of bandgaps (including avoided crossings) at different frequencies. The cut-off frequency of the 2nd longitudinal branch decreases and closes the longitudinal bandgap. More results are collected in Appendix B. One additional deaf mode appears for both epoxy and steel metastrips. The related modal distributions are shown in Figs. 7(a) and 8(a) (point I_1). Their vibrations are asymmetric with respect to the wave propagation direction. Hence they do not affect the transmission spectrum for a harmonic plane wave source. The viscoelastic model should be included in the numerical calculation whenever the viscosity of the medium can not be neglected. In this way, the experimental transmission can be well predicted by numerical simulations, as illustrated by Figs. 7(b) and 8(b).

It is observed in Fig. 8 that the lowest z-polarized bandgap exists at $20.2 - 22.6$ kHz for the I-type steel metastrip. The corresponding vibration modes at the band edges are also illustrated in the figure. It is observed that the modal distribution at the lower edge (point I_3) is similar to the second order flexural vibration of a simply supported beam in the xz-plane. The exterior ends of the narrow connectors and the central of the lump have almost no vibration. The vibration mode at the lower edge of H-type metastrip (point H_3 in Fig. 2) has similar characteristics. IT is thus not surprising that these two lower edge modes have almost identical frequencies. For the upper edge (point I_2), the modal distribution looks like the first-order flexural vibration of a beam with two free ends in the yz-plane. Similar pattern can also be found at the upper edge of the H-type metastrip in Fig. 2 (point H_2). However, the connectors support relatively large vibrations, leading to different upper band edges for the H-type and I-type metastrips.

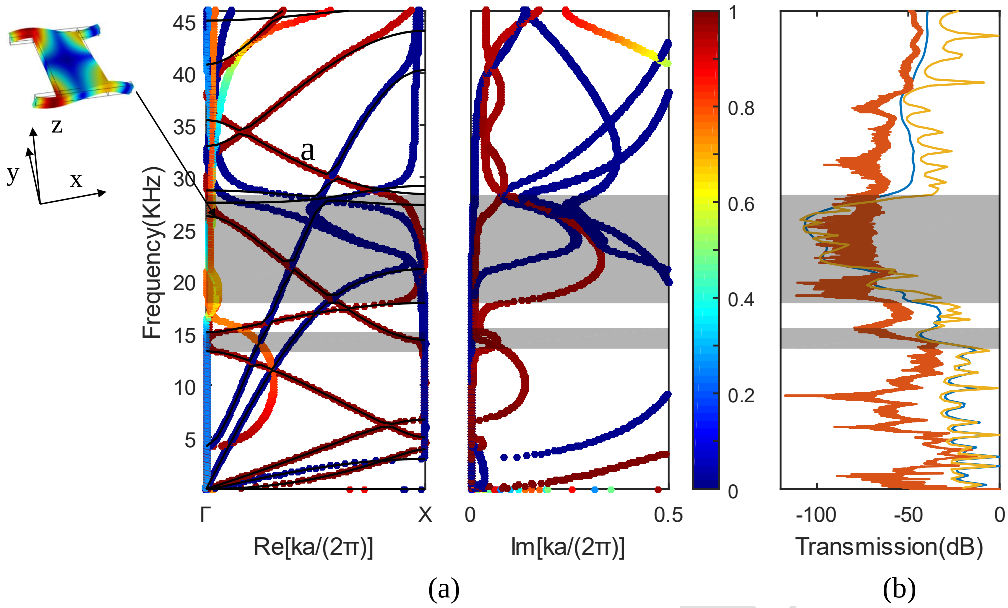

Figure 7: Complex band structure and transmission spectrum for the I-type epoxy metastrip. The left and right parts in panel (a) show the variation of frequency with the real and imaginary wave number, respectively. Viscosity is included using the K-V model. The color scale indicates the polarization of waves from in-plane modes (blue) to out-of-plane modes (red). The black solid line is for the real band structure of the corresponding elastic model. The gray area represents the band gap for out-of-plane waves in the real band structure. The inset shows the vibration mode of the z-polarized band inside the 2nd bandgap. Experimental transmission is represented in panel (b) with the red line. For comparison, the numerical transmission obtained using the K-V model and the corresponding elastic model are presented by the blue and the yellow lines, respectively.

VII. CONCLUSION

In this paper, we have investigated the propagation of evanescent Lamb waves in viscoelastic metastrips made of epoxy. With the aid of the finite element method, we have calculated the complex band structure and the transmission spectrum of the metastrip by taking the K-V model into account. Experiments were conducted to measure the transmission spectrum and the distribution of displacements. For comparison, the results for essentially lossless steel metastrips are also given. A theoretical model is proposed for the distribution of the displacements of evanescent waves. The effect of different slicing forms on the complex band structure and the transmission spectrum were also discussed. The results and discussions lead us to the following conclusions:

(1) In addition to propagating Lamb waves, evanescent Lamb waves in the elastic metastrip are precisely characterized by using the complex band structure. Deaf bands are observed for a symmetric z-polarized wave source. The numerical transmission obtained by using the elastic model agrees well with experiment for the elastic steel metastrip.

(2) When viscosity is introduced, all Lamb waves become evanescent in the viscoelastic epoxy metastrip. The numerical and experimental distributions of those evanescent waves can be predicted accurately by the proposed theoretical model, considering only the two least evanescent waves obtained from the complex band structure involving

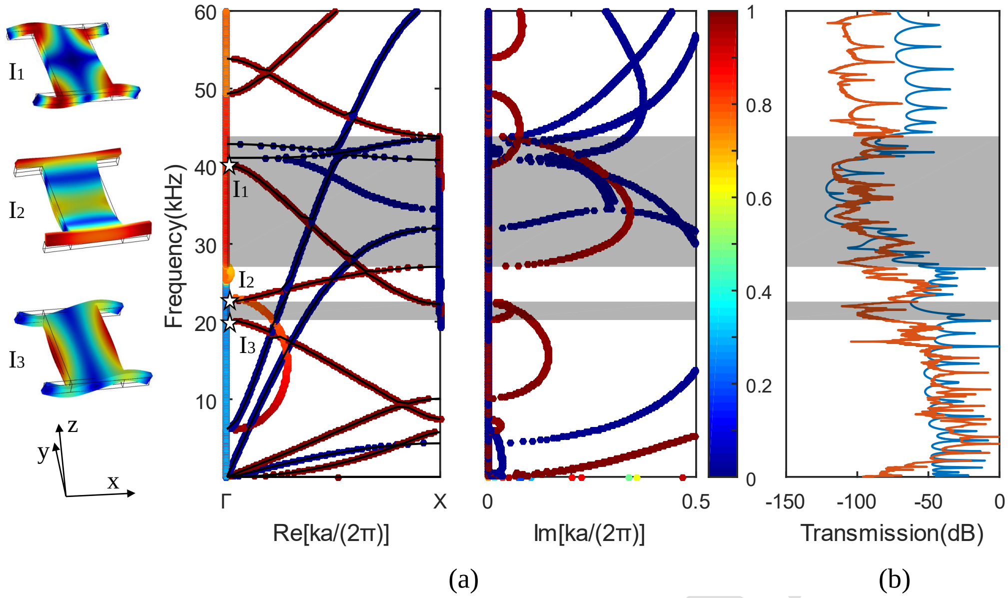

Figure 8: Complex band structure (a) and transmission spectrum (b) of the I-type steel metastrip. The left and right parts in panel (a) show the variation of frequency with the real and imaginary wave number, respectively. Only the elastic model is considered. The color scale indicates the polarization of waves from in-plane modes (blue) to out-of-plane modes (red). The black solid line is the real band structure of the elastic model. The gray area represents the band gap for out-of-plane waves. The insets show vibration modes of the z-polarized band at the marked points I_1, I_2 and I_3 in panel (a). Numerical and experimental transmissions are represented in panel (b) with the red and the blue lines, respectively.

the K-V model.

(3) Lamb wave propagation in the metastrip is highly affected by the choice of the cutting form defining the unit cell. Different cutting forms can result in the reconstruction of evanescent waves, leading to the opening or closing of bandgaps.

In addition to the phononic metastrip considered in this study, the proposed model can be extended to two-dimensional periodic metaslabs[19], and to metastructures with binary-phase media[71]. Novel devices based on viscoelastic metastrips are expected.

VIII. ACKNOWLEDGMENTS

Financial support from the National Natural Science Foundation of China (12122207, 12021002 and 11991032) is gratefully acknowledged. V.L. acknowledges support from the EIPHI Graduate School (ANR-17-EURE-0002).

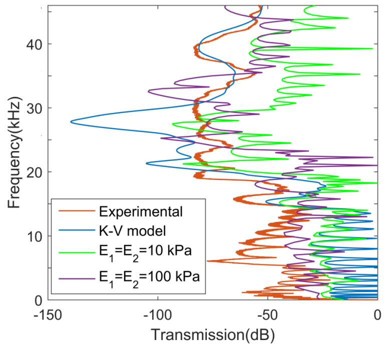

Figure 9: Transmissions of H-type epoxy metastrip calculated by using generalized Maxwell model (green and purple lines). For comparison, experimental transmission and numerical one obtained by the K-V model are presented with the red and blue lines, respectively.

Appendix A: NUMERICAL TRANSMISSION OBTAINED BY GENERALIZED MAXWELL MODEL

In addition to the K-V model, the generalized Maxwell model can be considered to calculate the transmission though the viscoelastic metastrip. The generalized Maxwell model has the following form:[47,53]:

$$E = E_0 + \sum_{n=1}^{m} E_n \frac{\omega^2 \tau_n^2}{1+\omega^2 \tau_n^2} + \imath \sum_{n=1}^{m} E_n \frac{\omega \tau_n}{1+\omega^2 \tau_n^2} \tag{A1}$$

where E is the complex-valued and frequency-dependent Young's modulus, E_0 is Young's modulus for the elastic case, E_n and τ_n denote the modulus contributions and the corresponding relaxation times, and m is the number of Maxwell elements. Of course, unless the parameters of the generalized Maxwell model can be fitted to experiment they can only be set rather arbitrarily. Here, we conduct the simulation by using $E_0 = 24$ GPa, $m = 2$, $\tau_1 = 1.2$, $\tau_2 = 0.1$. Results in Fig. 9 are plotted with green ($E_1 = E_2 = 10$ kPa) and purple ($E_1 = E_2 = 100$ kPa) lines, respectively. Although the decay frequency regions are observed to be close to the experimental results in the case of the green line, the exact transmission is not the same. When we increase E_1 and E_2, the transmission spectrum moves toward higher frequencies and consistency becomes even worse. Therefore, we do not find improved agreement with experiment when compared to the K-V model.

Appendix B: EFFECT OF CUTTING FORMS ON COMPLEX BAND STRUCTURE

In this appendix we present the complex band structure for metastrips with different cutting forms. Different metastrips are indeed obtained by translating the cutting planes along the y-axis in Fig. 6(a). I-type and H-type metastrips discussed in the main text are obtained for $y = 0$ and $y = 10$ mm, respectively. The complex band structure for metastrips obtained for $y = 3$ mm (Fig. 10(a)), and $y = 7$ mm (Fig. 10(b)) are considered here.

Comparing Figs. 4(a), 7(a) and 10, it is observed that the complex band structure is clearly different for different cutting forms. Fig. 7(a) shows that as y increases, the slope of band a changes first from negative to positive, and then becomes negative again. Besides, there is an intersection of two longitudinal bands for the H-type metastrip

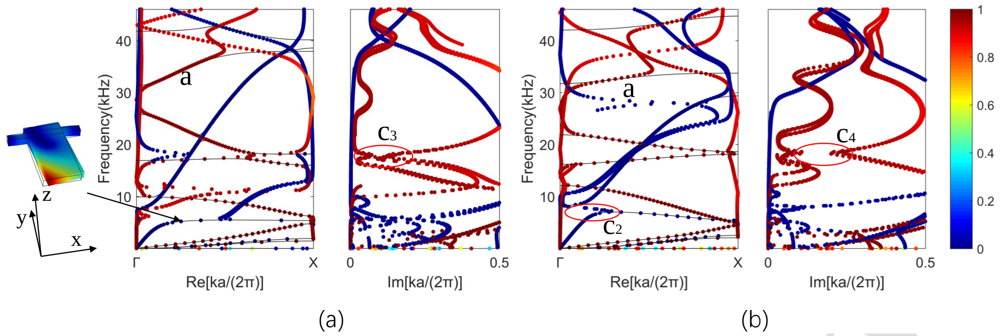

Figure 10: Complex band structure of metastrip obtained for cutting forms with (a) $y = 3$ mm and (b) $y = 7$ mm. The left and right parts in panel (a) and (b) show the variation of frequency with the real and imaginary wave number, respectively. The black solid line is the real band structure of the elastic model. The distributions of the z-polarized displacement at the marked points in panel (a) are also presented. The color scale indicates the polarization of waves from in-plane modes (blue) to out-of-plane mode (red).

($y = 10$ mm) in Fig. 4 (marked as circle c_1). As y decreases, the intersection separates. An avoided crossing appears in Fig. 10(b) (marked as circle c_2) for $y = 7$ mm. Furthermore, a resonant band gap appears in Fig. 10(a) for $y = 3$ mm. If y is further decreased down to 0, the lowest two longitudinal bands become almost parallel with each other, and the band gap disappears (as illustrated by Fig. 7 for the I-type metastrip). Moreover, it is also interesting to observe that different cutting forms can break the continuity of complex bands[61,72], leading to the reconstruction of evanescent waves (see circles c_3 and c_4 in Fig. 10).

---

* Electronic address: wangyanfeng@tju.edu.cn
1 M. M. Sigalas and E. N. Economou, Journal of Sound and Vibration **158**, 377 (1992).
2 M. S. Kushwaha, P. Halevi, L. Dobrzynski, and B. Djafari-Rouhani, Physical Review Letters **71**, 2022 (1993).
3 Z. Liu, X. Zhang, Y. Mao, Y. Zhu, Z. Yang, C. T. Chan, and P. Sheng, Science **289**, 1734 (2000).
4 M.-H. Lu, L. Feng, and Y.-F. Chen, Materials Today **12**, 34 (2009).
5 Y.-F. Wang, Y.-Z. Wang, B. Wu, W. Chen, and Y.-S. Wang, Applied Mechanics Reviews **72**, 040801 (2020).
6 M. Kafesaki and E. Economou, Physical Review B **52**, 13317 (1995).
7 R. Martínez-Sala, J. Sancho, J. Sánchez, V. Gómez, J. Llinares, and F. Meseguer, Nature **378**, 241 (1995).
8 J. V. Sánchez-Pérez, D. Caballero, R. Mártinez-Sala, C. Rubio, J. Sánchez-Dehesa, F. Meseguer, J. Llinares, and F. Gálvez, Physical Review Letters **80**, 5325 (1998).
9 Y. Tanaka and S.-i. Tamura, Physical Review B **58**, 7958 (1998).
10 C. Albino, L. Godinho, P. Amado-Mendes, P. Alves-Costa, D. Dias-da Costa, and D. Soares Jr, Engineering Structures **196**, 109340 (2019).
11 Q. Yang, T. Song, X.-D. Wen, H.-F. Zhu, Z.-H. Tan, L.-J. Liu, Z.-J. Liu, and X.-W. Sun, Physics Letters A **384**, 126885 (2020).
12 Y. Zeng, L. Cao, Y. Zhu, Y.-F. Wang, Q.-J. Du, Y.-S. Wang, and B. Assouar, Applied Physics Letters **119**, 013501 (2021).
13 M. S. Kushwaha, Applied Physics Letters **70**, 3218 (1997).
14 V. M. García-Chocano, S. Cabrera, and J. Sánchez-Dehesa, Applied Physics Letters **101**, 184101 (2012).
15 F. Morandi, M. Miniaci, A. Marzani, L. Barbaresi, and M. Garai, Applied Acoustics **114**, 294 (2016).
16 A. Colombi, P. Roux, S. Guenneau, P. Gueguen, and R. V. Craster, Scientific Reports **6**, 1 (2016).
17 Y. Zhang, W. Feng, and W. Che, 2016 IEEE International Conference on Microwave and Millimeter Wave Technology (ICMMT) **1**, 380 (2016).
18 A. Khelif, A. Choujaa, S. Benchabane, B. Djafari-Rouhani, and V. Laude, Applied Physics Letters **84**, 4400 (2004).
19 Y.-F. Wang, T.-T. Wang, J.-P. Liu, Y.-S. Wang, and V. Laude, Composite Structures **206**, 588 (2018).
20 B. Rostami-Dogolsara, M. K. Moravvej-Farshi, and F. Nazari, Journal of Molecular Liquids **281**, 100 (2019).

[21] Y.-F. Wang, L. Yang, T.-T. Wang, A.-L. Chen, V. Laude, and Y.-S. Wang, Apl Materials **9**, 081110 (2021).
[22] T.-G. Lee, S.-H. Jo, H. M. Seung, S.-W. Kim, E.-J. Kim, B. D. Youn, S. Nahm, and M. Kim, Nano Energy **78**, 105226 (2020).
[23] S.-H. Jo, H. Yoon, Y. C. Shin, W. Choi, C.-S. Park, M. Kim, and B. D. Youn, International Journal of Mechanical Sciences **179**, 105670 (2020).
[24] S.-H. Jo, Y. C. Shin, W. Choi, H. Yoon, B. D. Youn, and M. Kim, Nano Convergence **8**, 1 (2021).
[25] D. Caballero, J. Sánchez-Dehesa, C. Rubio, R. Martinez-Sala, J. Sanchez-Perez, F. Meseguer, and J. Llinares, Physical Review E **60**, R6316 (1999).
[26] S. Mukherjee and E. H. Lee, Computers & Structures **5**, 279 (1975).
[27] I. A. Veres, T. Berer, and O. Matsuda, Journal of Applied Physics **114**, 083519 (2013).
[28] R. Sprik and G. H. Wegdam, Solid State Communications **106**, 77 (1998).
[29] T. Suzuki and K. Paul, Journal of the Mechanics and Physics of Solids **46**, 115 (1998).
[30] V. Laude, Y. Achaoui, S. Benchabane, and A. Khelif, Physical Review B **80**, 092301 (2009).
[31] X. Ao and C. T. Chan, Physical Review B **80**, 235118 (2009).
[32] Y.-F. Wang, S.-Y. Zhang, Y.-S. Wang, and V. Laude, Physical Review B **102**, 144303 (2020).
[33] Y. Xiao, J. Wen, and X. Wen, Journal of Physics D: Applied Physics **45**, 195401 (2012).
[34] E. J. P. d. Miranda Jr and J. M. C. d. Santos, in *International Symposium on Dynamic Problems of Mechanics* (Springer, 2017), pp. 487–499.
[35] L. Han, Y. Zhang, Z.-Q. Ni, Z.-M. Zhang, and L.-H. Jiang, Physica B: Condensed Matter **407**, 4579 (2012).
[36] L. Liu and M. I. Hussein, Journal of Applied Mechanics **79** (2012).
[37] L. Airoldi and M. Ruzzene, New Journal of Physics **13**, 113010 (2011).
[38] M. Oudich and M. Badreddine Assouar, Journal of Applied Physics **112**, 104509 (2012).
[39] N. Gao, B. Wang, K. Lu, and H. Hou, Applied Acoustics **177** (2021).
[40] Y.-H. Cho, A. P. Pisano, and R. T. Howe, Journal of Microelectromechanical Systems **3**, 81 (1994).
[41] C. Goffaux and J. Sánchez-Dehesa, Physical review B **67**, 144301 (2003).
[42] M. I. Hussein, Physical Review B **80**, 212301 (2009).
[43] R. P. Moiseyenko and V. Laude, Physical Review B **83**, 064301 (2011).
[44] F. Farzbod and M. J. Leamy, Journal of Vibration and Acoustics **133** (2011).
[45] X.-y. Zhu, W.-q. Chen, and Z.-x. Yang, Journal of Materials in Civil Engineering **25**, 328 (2013).
[46] M. I. Hussein and M. J. Frazier, Journal of Sound and Vibration **332**, 4767 (2013).
[47] J. Li, P. Yang, Q. Ma, and M. Xia, Acta Mechanica **232**, 2933 (2021).
[48] J. Yi, Z. Li, M. Negahban, R. Xia, and J. Zhu, Mechanical Systems and Signal Processing **162**, 108101 (2022).
[49] M. Lewińska, V. Kouznetsova, J. Van Dommelen, A. Krushynska, and M. Geers, International Journal of Solids and Structures **126**, 163 (2017).
[50] M. Collet, M. Ouisse, M. Ruzzene, and M. Ichchou, International Journal of Solids and Structures **48**, 2837 (2011).
[51] A. Krushynska, V. Kouznetsova, and M. Geers, Journal of the Mechanics and Physics of Solids **96**, 29 (2016).
[52] J. Lou, L. He, J. Yang, S. Kitipornchai, and H. Wu, Applied Acoustics **141**, 382 (2018).
[53] A. O. Krushynska, A. S. Gliozzi, A. Fina, D. Krushinsky, D. Battegazzore, M. A. Badillo-Ávila, M. Acuautla, S. Stassi, C. Noè, N. M. Pugno, et al., Advanced Functional Materials **31**, 2103424 (2021).
[54] C. Ma, J. Guo, and Y. Liu, Journal of Physics and Chemistry of Solids **87**, 95 (2015).
[55] Y. Li, X. Zhou, Z. Bian, Y. Xing, and J. Song, Composite Structures **172**, 311 (2017).
[56] W. Witarto, K. B. Nakshatrala, and Y.-L. Mo, Mechanics of Materials **134**, 38 (2019).
[57] Y. Yao, F. Wu, Z. Xin, and Z. Hou, Physics Letters A **376**, 579–583 (2012).
[58] F.-C. Hsu, C.-I. Lee, J.-C. Hsu, T.-C. Huang, C.-H. Wang, and P. Chang, Applied Physics Letters **96**, 051902 (2010).
[59] E. Coffy, T. Lavergne, M. Addouche, S. Euphrasie, P. Vairac, and A. Khelif, Journal of Applied Physics **118**, 214902 (2015).
[60] T.-T. Wang, Y.-F. Wang, Y.-S. Wang, and V. Laude, Applied Physics Letters **111**, 041906 (2017).
[61] Y.-F. Wang, Y.-S. Wang, and V. Laude, Physical Review B **92**, 104110 (2015).
[62] A. Palermo and A. Marzani, International Journal of Solids and Structures **191**, 601 (2020).
[63] D. Yu, J. Wen, H. Zhao, Y. Liu, and X. Wen, Journal of Sound and vibration **318**, 193 (2008).
[64] V. Laude, Y. Achaoui, S. Benchabane, and A. Khelif, in *IUTAM Symposium on Recent Advances of Acoustic Waves in Solids* (Springer, 2010), pp. 165–173.
[65] Y.-F. Wang, Y.-S. Wang, and X.-X. Su, Journal of Applied Physics **110**, 113520 (2011).
[66] V. Laude, R. P. Moiseyenko, S. Benchabane, and N. F. Declercq, AIP Advances **1**, 041402 (2011).
[67] V. Romero-García, L. M. Garcia-Raffi, and J. V. Sánchez-Pérez, Aip Advances **1**, 041601 (2011).
[68] V. Romero-García, J. V. Sánchez-Pérez, S. Castiñeira-Ibáñez, and L. Garcia-Raffi, Applied Physics Letters **96**, 124102 (2010).
[69] Y.-F. Wang, T.-T. Wang, J.-W. Liang, Y.-S. Wang, and V. Laude, Journal of Sound and Vibration **437**, 410 (2018).
[70] D. Feng, D. Xu, G. Wu, B. Xiong, and Y. Wang, Applied Physics Letters **103**, 151906 (2013).
[71] Y.-F. Wang, J.-W. Liang, A.-L. Chen, Y.-S. Wang, and V. Laude, Physical Review B **101**, 184301 (2020).
[72] V. Laude, J. M. Escalante, and A. Martínez, Physical Review B **88**, 224302 (2013).

Highlights

- Complex band structure for evanescent Lamb waves is calculated by using finite element method.
- Numerical and experimental distributions of evanescent waves agree well and can be accurately predicted.
- Evanescent waves are reconstructed for different cutting forms, leading to the opening or closing of bandgaps.

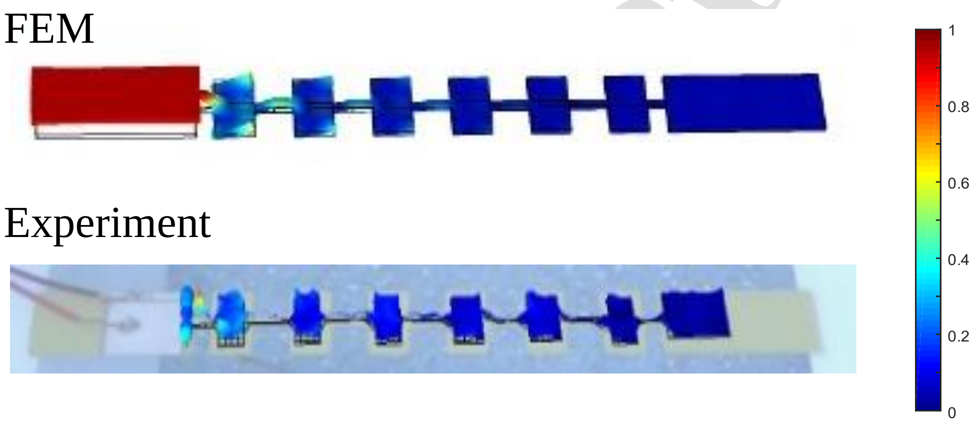

Attenuation of evanescent waves in the H-type epoxy metastrip

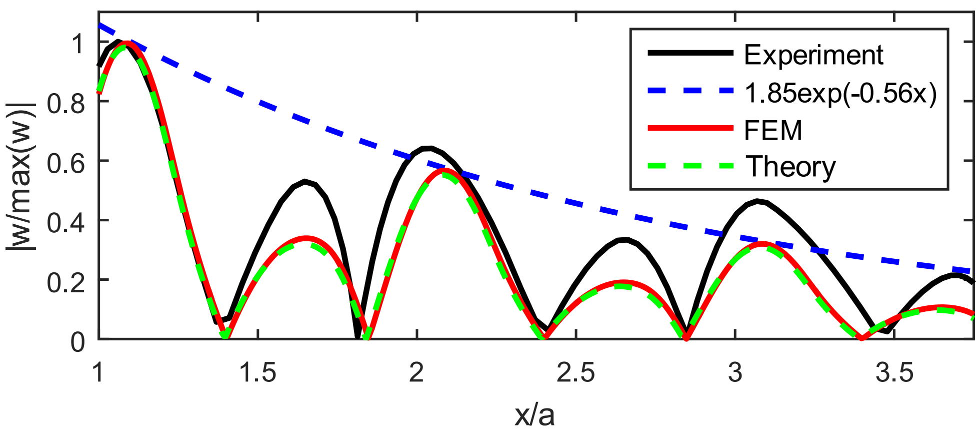

The numerical, experimental and predicted displacement distributions of evanescent waves

Author statement

Wei Guo: Methodology, Software, Writing- Original Draft; Shu-Yan Zhang: Validation; Yan-Feng Wang: Conceptualization, Supervision, Writing-Reviewing and Editing; Vincent Laude: Writing-Reviewing and Editing; Yue-Sheng Wang: Writing-Reviewing and Editing.

Declaration of interests

☒ The authors declare that they have no known competing financial interests or personal relationships that could have appeared to influence the work reported in this paper.

☐The authors declare the following financial interests/personal relationships which may be considered as potential competing interests: